ADVANCING EARTH AND SPACE SCIENCES

JGR Planets

RESEARCH ARTICLE

10.1029/2024JE008696

The Hermean Helium Exosphere—Continuous and Sporadic Helium Release Processes

J. Hener[1,2], **P. Wurz**[1], **F. Weichbold**[3], **H. Lammer**[3], **D. Schmid**[3], **and A. Vorburger**[1]

[1]Space Research and Planetary Sciences, Physics Institute, University of Bern, Bern, Switzerland, [2]Faculty of Aerospace Engineering, Delft University of Technology, Delft, The Netherlands, [3]Space Research Institute, Austrian Academy of Sciences, Graz, Austria

Key Points:

- We present results from an ab-initio model of the steady state Helium exosphere
- Comparison of model and measurements confirms that the measurable Helium exosphere is dominated by the flux of thermally recycled Helium
- Sporadic release events (meteorite impacts) can overcome the steady-state Helium background, yet the in situ detection probability is small

Correspondence to:

J. Hener,
j.hener@tudelft.nl

Citation:

Hener, J., Wurz, P., Weichbold, F., Lammer, H., Schmid, D., & Vorburger, A. (2025). The Hermean Helium Exosphere—Continuous and sporadic Helium release processes. *Journal of Geophysical Research: Planets*, *130*, e2024JE008696. https://doi.org/10.1029/2024JE008696

Received 3 SEP 2024
Accepted 17 MAR 2025

Author Contributions:

Conceptualization: J. Hener, P. Wurz, A. Vorburger
Data curation: F. Weichbold, H. Lammer, D. Schmid
Formal analysis: J. Hener, F. Weichbold, H. Lammer, D. Schmid, A. Vorburger
Funding acquisition: P. Wurz
Methodology: J. Hener, P. Wurz, A. Vorburger
Project administration: P. Wurz
Resources: F. Weichbold, H. Lammer, D. Schmid
Software: J. Hener, P. Wurz, A. Vorburger
Supervision: P. Wurz, A. Vorburger
Validation: J. Hener, A. Vorburger
Visualization: J. Hener
Writing – original draft: J. Hener
Writing – review & editing: J. Hener, P. Wurz, A. Vorburger

Abstract

Since its detection by Mariner 10, helium has been a key focus in studies of Mercury's exosphere. Recently, Weichbold et al. (2025), https://doi.org/10.1029/2024je008679 provided the first in situ helium measurements, inferring density from Ion Cyclotron Wave (ICW) events observed by the MESSENGER spacecraft. This approach enables, for the first time, a helium density profile across a broad altitude range without relying on prior models. We present an ab-initio model for a steady state, solar wind-driven helium exosphere, which informed the interpretation of these ICW measurements. We discuss helium release processes and evaluate whether meteoroid impacts could account for specific instances of elevated helium measurements. We developed a global, semi-analytical model based on a helium-saturated regolith and an average helium source flux of $2.5^{+2.5}_{-1.25} \times 10^{23}$ He/s from solar wind ion implantation. We calculate the helium flux distribution using an analytical lateral transport model and then generate local radial density profiles from a numerical (Monte Carlo) radial transport model. Additionally, we applied the radial transport model to estimate the scale and duration of large, sporadic helium release events and assess the likelihood of detecting these events in situ. The strong agreement between our model and the novel measurements confirms that the measurable helium exosphere is dominated by thermally recycled particles. We show that elevated helium measurements can result from the vaporization and release of helium from large (1 m) meteoroid impacts, but it is statistically unlikely that more than one impact event is captured in the given set of measurements.

Plain Language Summary

Helium is a key element in Mercury's thin atmosphere, first discovered by the Mariner 10 mission. Recent studies used data from the MESSENGER spacecraft to directly measure helium abundance locally, offering a detailed view of how it is distributed at different altitudes without relying on pre-existing models. This research presents a model to explain these observations, showing that most of Mercury's helium comes from particles introduced by the solar wind, which then have a long lifetime in the atmosphere. The study also explores whether large meteoroid impacts could explain spikes in the measured helium levels, but finds that such events are rare and unlikely to account for multiple high readings.

1. Introduction

Despite being considered an atmosphere-less planetary body, Mercury hosts a thin atmosphere, or more specifically a surface bound exosphere. Through the study of the hermean exosphere and the processes, which define its interaction with the planetary surface and the space environment, important insights about the surface bulk properties and the environment can be derived (Wurz et al., 2022).

Since its original detection by Mariner 10 (Broadfoot et al., 1974), helium and its role in the hermean exosphere has been discussed extensively. With the UV Spectrometer measurements from Mariner 10, Broadfoot et al. (1974) first measured the vertical column density and constrained the surface number density. Hartle et al. (1975) used a model fit to establish an exospheric helium supply of 6.8×10^{22} He/s. Goldstein et al. (1981) use an ab-initio approach to discuss He source processes and their strengths and show that the helium supply may in fact be larger. Leblanc and Chaufray (2011) fit different models to the same Mariner 10 data and derive a helium source strength of $(2.4–5.0) \times 10^{23}$ He/s. All of these source rates are compatible with helium supply from precipitating solar wind He^{++} ions. Goldstein et al. (1981) found that the contribution of outgassing of radiogenic helium was limited to a maximum of 4×10^{22} He/s, approximately an order of magnitude smaller than the required source strength. While solar wind seems to be the much more influential driver for the helium exosphere, there is still no observationally backed analysis on the relative importance of solar wind ion precipitation and competing mechanisms.

Most recently, Weichbold et al. (2025) added the first set of in situ He measurements to the picture. They report their measurement technique, in which they infer the neutral helium density from the intensity of so-called Ion Cyclotron Wave (ICW) events in the magnetic field measurements of the MESSENGER spacecraft. These in situ abundance measurements over an extended altitude range allow for the first time to retrieve an He exosphere density profile without making model assumptions a priori. Weichbold et al. (2025) show that the majority of their measurements are consistent with a thermal helium exosphere of solar wind origin. In addition, they attribute some measurements to potential meteoroid impact events. In this paper we provide the details for the ab-initio model for a steady state, solar wind implantation driven helium exosphere, which was used in the interpretation of the measurements (see Weichbold et al., 2025). We discuss the importance of various release processes and examine if meteoroid impacts are a plausible source of the individual measurements of enhanced helium abundances reported by Weichbold et al. (2025).

We report our work in two main sections. In Section 2 we present our cross-seasonal average steady-state model and compare model results to the ICW-derived He density measurements. With Section 3 we follow up on the findings of this comparison and investigate the creation and detection probability of meteoroid impact signatures in the helium exosphere. In Section 4 we close with a presentation of our main conclusions.

2. Steady-State Model

The hermean exosphere is a dynamic system, responding to changes in orbital position (hermean season), local time (hermean day), and solar wind conditions (Wurz & Lammer, 2003). The helium abundance measurements, which Weichbold et al. (2025) inferred from ICW events, were collected over a span of 4 years (2011–2015) and cover a wide range of dayside local times. The measured quantity is therefore expected to undergo substantial fluctuations. In this section we present an ab-initio model of the hermean helium exosphere, which we build for the comparison with the helium abundance measurements from Weichbold et al. (2025). It is based on averaged environmental quantities and is meant to reflect a cross-seasonal average steady state of the helium exosphere over the dayside.

In Section 2.1 we discuss the source and sink processes that act within the hermean helium environment. In Sections 2.2 and 2.3 we present our modeling of the radial and lateral transport of exospheric helium. Section 2.4 shows how the different modeling approaches are combined into a global, semi-analytical model for the helium distribution around Mercury. Lastly, Section 2.5 shows how the model results compare to the ICW-inferred abundance measurements.

2.1. Processes in the Hermean Helium Exosphere

2.1.1. Exospheric Source Flux

It is widely accepted that the primary source of helium in the hermean environment is the solar wind (Goldstein et al., 1981; Killen et al., 2007). Solar wind He^{++} ions precipitate onto the surface, where a large fraction of them is implanted into the regolith as neutral helium. Typical implantation depths in surface analogs are reported in the order of tens of nm (Lord, 1968), thus well beyond the first atomic layers of the surface structure. Through gardening of the regolith, regolith grains with implanted helium can be transported to much larger depths, as is demonstrated by the presence of solar wind implanted He at a few meters depth in the lunar regolith (Bogard et al., 1973; Wittenberg et al., 1986). By further analogy with lunar regolith (Jull & Pillinger, 1977), we assume, like many authors before, that hermean regolith is saturated with helium, in the sense that the flux of implanted He matches the flux of released He from the grain. As noted by Goldstein et al. (1981), saturation may not be given for the entire hermean surface, but certainly applies to the nightside and also on the high-latitude dayside cusps, where typically a large part of the solar wind ion precipitation occurs, see review by Wurz et al. (2022). The mechanisms underlying the interaction between precipitating He^{++} ions and the saturated surface structure, as well as the nature of the helium release process are not yet understood. The work of Goldstein et al. (1981) includes an extensive discussion on the topic, ruling out sputtering and micrometeoroid erosion, but considering diffusion and diffusion related mechanisms as feasible options for the release of helium from the regolith grains. With this work we do not aim to further contribute to this discussion. Like previous works of for example, Hartle et al. (1975), we conclude that in a typical, global steady-state scenario precipitating He^{++} ions encounter He saturated regolith and that the precipitation flux directly acts as a source of exospheric neutral helium.

The efficiency at which Mercury intercepts solar wind ions and allows precipitation onto the surface varies as a function of solar wind pressure and orientation of the interplanetary magnetic field (IMF) (Fatemi et al., 2020; Kallio & Janhunen, 2003; Massetti et al., 2003). Using MESSENGER plasma data, Winslow et al. (2012) estimate that $(1.1 \pm 0.6) \times 10^{24}$ protons per second bombard the surface over an area of $(5.2 \pm 1.6) \times 10^{11}$ m^2 near the northern cusp centered at 74.7° Mercury Solar Orbital latitude on the surface. This gives a solar wind flux of 2.11×10^{12} m^{-2} s^{-1} onto the northern cusp, which agrees with earlier theoretical estimates within a factor 2 (Kallio & Janhunen, 2003; Massetti et al., 2003). From the ratio of the surface field strength in the south to that in the north pole, Winslow et al. (2012) estimate that the cusp area in the south extends over 2×10^{12} m^2, thus the number of ions reaching the surface in the southern cusp region is correspondingly higher, 4×10^{24} particles per second (Winslow et al., 2012). This gives in total 5.1×10^{24} protons/s hitting Mercury's surface. Assuming a He^{++} fraction of 5% in the solar wind this results in 2.5×10^{23} He^{++}/s hitting Mercury's surface. Given our goal to create an average steady-state model, we adopt a mean value of 2.5×10^{23} s^{-1} for the average global He^{++} precipitation rate.

There are additional mechanisms which modulate the intensity of precipitating ions and the efficiency with which they implant and thus trigger the release of helium from the saturated regolith. About 16% of the precipitating solar wind ions are back-scattered from the (lunar) surface as energetic neutral particles (Vorburger et al., 2013) and lost from the exosphere, and about 1% is typically back-scattered as ions (Lue et al., 2011, 2014). These back-scattered particles do not count toward the supply of the neutral exosphere. From the implantation experiment onboard the Genesis mission, it was found that a fraction of 10%–60% (Grimberg et al., 2009) is implanted in the target materials (*AloS* (aluminum on sapphire), *DOS* (diamond-like carbon on silicon), *Si* (silicon) and *BMG* (bulk metallic glass). Of course, these materials might not be representative for the granular and porous structure of the regolith. At the same time, a fraction of the exospheric helium is precipitating back to the surface after undergoing ionizing processes and therefore intensifies the effective ion precipitation. Goldstein et al. (1981) estimate the fraction of recycled helium ions between 0% and 50%. The uncertainties on these contributions are immense and testify to the difficulty in quantifying these processes. Therefore we treat them as secondary mechanisms and do not explicitly factor them into our analysis. This is not to say that they do not contribute measurably to the helium exosphere, but due to the lack of knowledge we equate the modulated effective precipitation flux to the average 2.5×10^{23} s^{-1} global precipitation rate.

Similarly, we do not explicitly account for an exospheric supply from radiogenic outgassing from the planetary interior. Goldstein et al. (1981) estimate the rate of such supply to be between 6.9×10^{21} and 4×10^{22} s^{-1}, so significantly below the ion precipitation rate. The same applies to the supply rate from interstellar neutral wind, which Broadfoot et al. (1976) estimate at 2×10^{21} s^{-1}, but later publication (e.g., Quémerais et al., 2023) quote at 0.1×10^{23} s^{-1} to 1×10^{23} s^{-1}, depending on the position of Mercury in its orbit. While the maximum interplanetary He flux is comparable in order of magnitude to the dominant He source, it has to be noted that this maximum value peaks very sharply only when Mercury crosses through a narrow cone of gravitationally focussed helium wind. The characteristic scale time of the He exosphere, which can be interpreted as the global exosphere's inertia to variations in particle influx or loss rates, is at least 10 days (Quémerais et al., 2023) or more (see Section 2.5), so when averaging the flux profile over this time span the peak He wind influx is flattened significantly to 0.6×10^{23} s^{-1} or less.

Concluding the discussion of the helium source processes, we apply a generous confidence interval of ± factor 2 around our modeled He source flux. This interval accommodates the uncertainties on the adopted solar wind precipitation flux quoted by Winslow et al. (2012) as well as other estimates by for example, Kallio and Janhunen (2003) and Massetti et al. (2003). The generous nature of the confidence interval also allows us to absorb the uncertain contributions from the secondary source processes, local modulations and flux variations over timescales of tens of days, that were discussed above. In summary, we model the helium source rate with the value of the average solar wind ion precipitation rate under consideration of a ± factor 2 uncertainty:

$$\begin{aligned} \Phi_S &= \Phi_{SW} \\ &= 2.5\,^{+2.5}_{-1.25} \times 10^{23} s^{-1} \end{aligned} \quad (1)$$

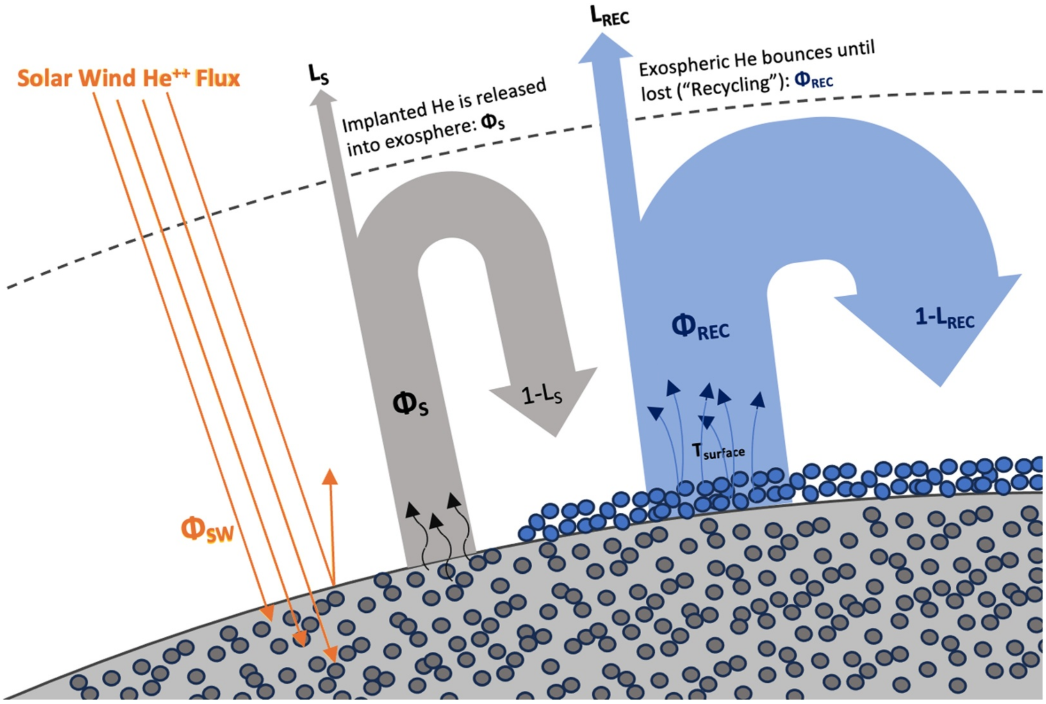

Figure 1. Schematic illustration of the main processes in our model. Solar wind precipitation delivers He^{++} ions to the system, which it implants as neutral helium in the regolith. The helium source flux Φ_S from the surface is in response to the ion precipitation onto the helium saturated surface and releases helium from the regolith into the exosphere. After its original release trajectory, each particle bounces a large number of times, where each time the He atoms are reemitted with an energy consistent with the local surface temperature and put on a new trajectory. This process of exospheric recycling is represented by Φ_{REC}. Note that the steady-state assumption of our model demands the balance between incoming and outgoing helium at two virtual borders: (a) At the surface the implantation rate has to equal the release rate and (b) at the system boundaries the solar wind helium supply rate has to equal the sum of all helium loss processes.

where Φ_S is the exospheric helium source flux and Φ_{SW} is the solar wind He^{++} precipitation flux. Equation 1 constitutes the balance between implanted and released helium at the surface boundary of our steady-state exosphere model (compare to Figure 1).

After release from the surface, source flux particles are modeled to be on collision-less ballistic trajectories, which are either lost from the exosphere by gravitational escape or photo-ionization, or return to the surface eventually (Wurz & Lammer, 2003). We do not need to specify the exact spatial distribution of the released flux, because the exospheric density distribution is only very weakly dependent on the origin of the particles (Hartle et al., 1975; Leblanc & Chaufray, 2011). We use for the energetic distribution of the source flux a thermal distribution with an average surface temperature, because the fraction of exospheric retention of this source population is much larger than the fraction of He atoms that are lost, that is, the He atoms will bounce thousand times on the surface before they are lost from the exosphere. We only consider thermal release and micrometeoroid impact vaporization, but no higher-energetic release mechanisms (photon-stimulated desorption and sputtering), because the latter are incompatible with the data, as discussed below.

2.1.2. Recycling Flux

Due to its properties as an inert gas, the retained helium atoms do not adsorb upon their return to the surface. Instead they undergo"exospheric recycling", in which upon each encounter with the surface the retained particles interact with the uppermost surface layer on very short timescales and are subsequently re-emitted onto ballistic trajectories.

Similar to the release mechanisms discussed in Section 2.1.1, the exact nature of the surface interaction and especially to what extent the particle thermalizes with the local surface, has been a topic of great debate (Broadfoot et al., 1976; Leblanc & Chaufray, 2011; Shemansky & Broadfoot, 1977; G. R. Smith et al., 1978).

Leblanc and Chaufray (2011) showed that neither full nor partial thermal accommodation models are able to explain the spatial distributions obtained from Broadfoot et al. (1976). We adopt a full thermal accommodation model. The issues with the spatial distribution are addressed by decoupling lateral and radial transport in a semi-analytical fashion (Sections 2.2 and 2.3).

The intensity of the exospheric recycling can be derived in two manners: Like for example, Hartle et al. (1975); Leblanc and Chaufray (2011) one can use a 3D Monte Carlo simulation to computationally determine the typical lifetime of thermal helium particles $(\bar{t}_{\text{life}})$ and compare it to the average particle flight time $(\bar{t}_{\text{flight}})$. As we demonstrate later, this ratio is in the order of a few thousand, meaning that over its lifetime the individual thermal helium atoms encounters the surface thousands of times, or that for each source flux particle there are a few thousand particles undergoing exospheric recycling:

$$\Phi_{\text{REC}} = \Phi_{\text{S}} \cdot \frac{\bar{t}_{\text{life}}}{\bar{t}_{\text{flight}}} \tag{2}$$

Equivalently, one can consider the steady-state condition at the boundary of the hermean system (including body and exosphere), where the exospheric loss has to balance the flux of incoming particles (compare to Figure 1). We already know that the recycling flux is orders of magnitude larger than the source and conclude that the recycling flux drives the exospheric loss. With a given particle distribution (Section 2.3) for the recycling flux and the ability to compute local escape and ionization loss fractions (Section 2.2), an effective global loss fraction $(L = L_{\text{REC}})$ can be established. The steady-state condition at the hermean system boundary then demands that the intensity of the recycling flux satisfies the exospheric loss for the given global loss fraction:

$$\Phi_{\text{REC}} = \Phi_{\text{SW}} \cdot \frac{1}{L_{\text{REC}}} \tag{3}$$

Note that because of Equation 1 and

$$\frac{1}{L} = \frac{\bar{t}_{\text{life}}}{\bar{t}_{\text{flight}}}$$

the expressions Equation 2 and Equation 3 for the exospheric recycling flux are equivalent.

2.2. Radial Transport

A 1D Monte Carlo Code (Wurz et al., 2010; Wurz & Lammer, 2003) is used to model the local radial transport of helium. A population of test-particles is initiated with a initial velocity distribution at surface level. For a population of thermally accommodated, recycled particles the initial velocity distribution is a Maxwell-Boltzmann distribution defined by the local surface temperature. From its initial state on the surface each test-particle is propagated on ballistic trajectories until it either escapes, is photo-ionized and lost, or returns to the surface. Due to the collision-less nature of exospheres, interactions between the particles are not modeled. From the statistics of the test-particles, a one-dimensional radial distribution profile can be retrieved. By knowledge of the local surface particle density (see Section 2.3) or radial column density, the distribution profile can be converted to physical particle number density.

So for a given particle species (He), particle surface density n_0 and surface temperature T_0, the Monte Carlo Code allows us to obtain the local number density as a function of altitude:

$$n_0, T_0 \xrightarrow{MC(\text{He})} n(h) \tag{4}$$

Additionally, the Monte Carlo code returns the local loss fractions for gravitational escape and photo-ionization, which are primarily a function of the initial velocity distribution and the photo-ionization rate. The rate is a product of a species' photo-ionization cross-section and the available flux of ionizing photons. While the former can be considered constant for a species and band of ionizing wavelengths, the latter varies with solar activity. Variations in solar activity would thus translate into the ionization rate, which is linearly related to the ionization loss fraction computed in our lateral transport code. We use a value of $6 \times 10^{-8}\ \mathrm{s}^{-1}$, consistent with the onset of the relatively quiet solar cycle 24 during the measurement period (Huebner & Mukherjee, 2015). The solar ionization rates of Helium can increase up to a factor 2 when large regions of strong activity arise (Huebner & Mukherjee, 2015; E. V. Smith & Gottlieb, 1974). However, the active regions are local, suggesting that possible peak ionization rates are modulated by the sun's 24 days rotation period and therefore act less significantly on the Mercury system.

$$n_0, T_0 \xrightarrow{MC(\mathrm{He})} L'_{\mathrm{ion}}, L'_{\mathrm{esc}} \tag{5}$$

2.3. Lateral Transport

Lateral transport mechanisms for helium on Mercury, which drive the surface number density distribution, are not well understood. 3D Monte Carlo exosphere models have failed to spatially distribute helium in a way that is consistent with the Mariner 10 observations (Leblanc & Chaufray, 2011; Shemansky & Broadfoot, 1977; G. R. Smith et al., 1978). When assuming full thermalization of helium upon interaction with the surface, these models produce day-night asymmetries of 1/100 to 1/200, while Mariner 10 observations call for much smaller asymmetries (Broadfoot et al., 1976). This is an unresolved problem, which we do not address. Instead, we use the analytical model for the lateral transport of gases in planetary exospheres, developed by Hodges Jr. and Johnson (1968). In this model, the particle surface density distribution is strictly a function of surface temperature:

$$n \cdot T^{5/2} = \mathrm{const} \tag{6}$$

We adopt an exponential cosine model for the surface temperature:

$$T_{0(\theta,\phi)} = 635 \cdot (\sin\theta \cos\phi)^{1/4}\ [^\circ\mathrm{K}] \tag{7}$$

where 635 K is the cross-seasonal average sub-solar surface temperature when the surface is in radiative equilibrium (Chase Jr. et al., 1976).

It should be noted that the hermean helium exosphere does not strictly comply with the validity criteria of the Hodges Jr. and Johnson (1968) lateral transport model. The decisive criterion $\epsilon > 15$, where $\epsilon = \left(V^2_{\mathrm{escape}}\right) / V^2_{\mathrm{thermal}}$ is a proxy for the average distance traversed in the exosphere by individual trajectories. For the exospheric helium population on Mercury this value varies from 44 over the nightside to a value of 5.6 on the dayside, implying that the criterion is not strictly met over the dayside. This was previously mentioned by Leblanc and Chaufray (2011), who furthermore pointed out that in such a scenario use of Equation 6 would result in an exaggerated day-night asymmetry. However, when using the analytical lateral transport relation in Equation 6 with the temperature profile of Equation 7, it results in a day-night asymmetry of 1/80, which is still in better agreement with the existing observations than any 3D MC model calculating the 3D He distribution directly. The corresponding surface number density distribution as well as column density and particle flux along the equator are shown in Figure 2.

By inspection of the equatorial surface number distribution in Figure 2 it can be noted that it is qualitatively very similar to equatorial profiles from the 3D Monte Carlo simulations of for example, Hartle et al. (1975) and G. R. Smith et al. (1978), only the day-night asymmetry is less pronounced. Another difference lies in the steepness of the density drop-off over the terminators. The drop-off in the analytical distribution goes strictly with the local temperature and is thus very sharp. In the MC distributions from for example, Hartle et al. (1975) and G. R. Smith et al. (1978), terminator gradients are smoother, indicating that the physical particle distribution may decouple somewhat from the local temperature when temperature gradients get too steep. In this regard the MC derived distribution seems more realistic. Since we do not attempt to model the terminator region in much detail, this shortcoming of the analytical is not expected to have a significant impact on the remainder of this work. Due to the lack of more applicable alternatives, we use the analytical model from Hodges Jr. and Johnson (1968) (Equation 6, Figure 2) to determine the surface density distribution in our exospheric helium model.

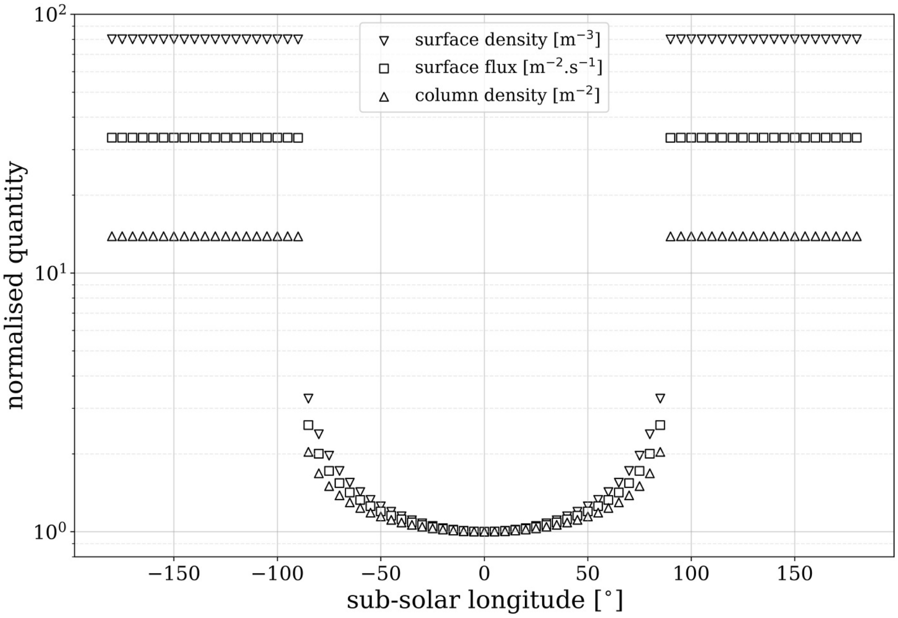

Figure 2. Normalized surface density distribution, column density distribution, and surface flux distribution along the equator, following the analytical surface distribution model in Equation 6 with the temperature model of Equation 7.

2.4. Synergy

To synthesize all previously presented aspects into one global model, we begin with considering the normalized helium distribution over the hermean surface (Equation 6, Figure 2). We divide the surface in elements of $5° \times 5°$. Using the resulting flux distribution, we can determine the fraction of the global helium flux on each surface element. We calculate the loss fraction (Equation 5) of the flux on each surface element and weigh it with its contribution to the total flux, which yields an effective global loss fraction L of 0.98×10^{-4}, with loss due to ionization and gravitation contributing 4.55×10^{-5} and 5.28×10^{-5}, respectively. The approximately equal loss between the two loss mechanisms is consistent with the results from recent 3D Monte Carlo simulations (Leblanc & Chaufray, 2011). After conversion of the loss fractions to the global loss rates, we report an ionization loss rate of 1.16×10^{23} He/s and an escape loss rate of 1.34×10^{23} He/s, which is within a few percent from the values reported by Leblanc and Chaufray (2011).

Having quantified the global loss fractions allows us to solve for the intensity of the recycling flux Φ_{REC} as given by Equation 3, which constitutes the effective global flux intensity of helium on the surface of Mercury. Using the effective global flux intensity and comparing to the integrated normalized flux distribution over all surface elements, we can scale the normalized distribution profiles to match the global helium flux intensity. This yields the surface number density (n_0), column density (N) and surface flux (Φ) on each surface element. Table 1 shows these values for selected surface locations. Note that the distribution of the total helium flux over the hermean surface according to Equation 6 results in dayside surface densities around 1×10^9 m^{-3}, which is consistent with densities derived from observations, from Mariner 10 for example, 1.5×10^9 m^{-3} by Hartle et al. (1975), 4.5×10^9 m^{-3} by Broadfoot et al. (1976), and from BepiColombo (0.625–1.0) *x* 10^9 m^{-3} by Quémerais et al. (2023).

Table 1
Temperature (T_0), Surface Number Density (n_0), Surface Flux (Φ) and Column Density (N) on Selected Surface Elements

	(0°, 0°)	(0°, 30°)	(0°, 180°)
T_0 (K)	635	615	110
n_0 [m^{-3}]	1.027×10^9	1.106×10^9	82.25×10^9
Φ [$m^{-2}s^{-1}$]	1.883×10^{12}	1.998×10^{12}	62.75×10^{12}
N [m^{-2}]	4.663×10^{14}	4.875×10^{14}	64.67×10^{14}

Note. Surface elements are of size $5 \times 5°$ and are given by the coordinates of their central point (lat, sub-solar lon). Uncertainties in the He source strength (Equation 1) translate linearly into the values presented below.

Using our MC radial transport model (Section 2.2, Equation 4) we can now compute the radial density profile over each surface element, which in sum constitutes our global model for the Mercury exosphere in steady state. As mentioned in Section 2.3, the model is not suitable for the study of the terminator region. Due to the effective decoupling of radial and lateral transport, this model will produce almost discontinuous changes in the exospheric structure over the terminator. In reality there will be mixing and

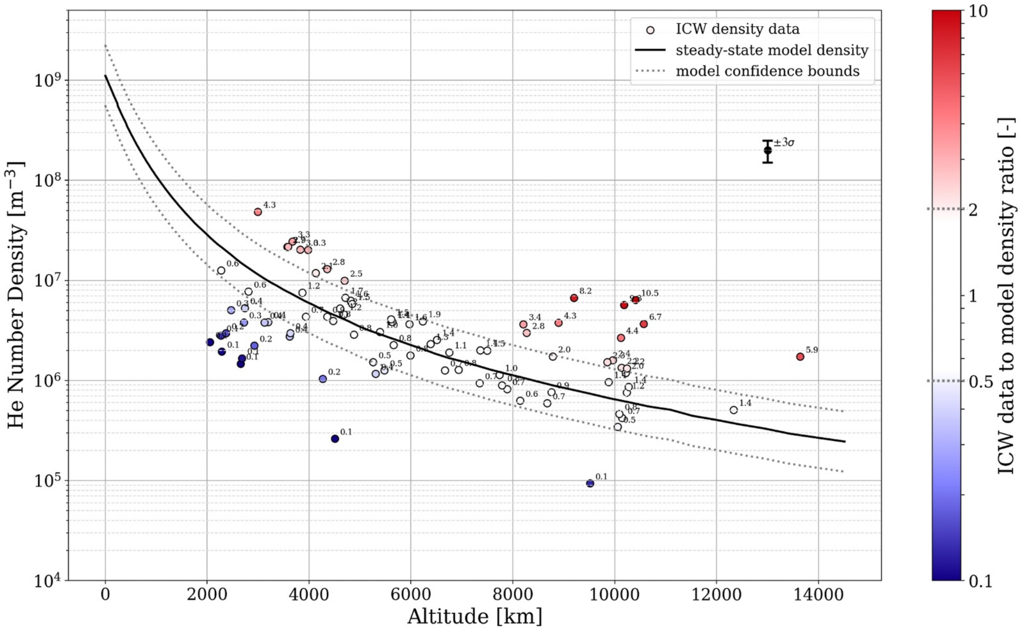

Figure 3. Dayside density profile from the steady state model compared to the ICW-derived helium measurements (from 03/2011 to 04/2015). Confidence bounds in the model result from uncertainties in the steady-state He influx and loss rates, as well as variations of sufficiently long timescales (>10 days). Measurement error (±25%) is illustrated using a dummy data point at (13,000, 2.0×10^8). Note that model and data were derived strictly separately, and no fitting has taken place. Also note that largest differences (≈ factor 10) between model curve and measurements occur at $9{,}000 < h < 11{,}000$ km.

”spilling over” of the particle flux from the day- and nightside surface elements in the terminator region, resulting in a smoother transition of the exosphere structure over the terminator.

We consider the numbers presented in Table 1 as cross-seasonal average steady state of the dayside and nightside helium exosphere. We extract the radial profile over the (0°, 30°) surface element and consider it representative of the dayside helium exosphere, and thus suitable for comparison with the dayside ICW density measurements (Section 2.5).

2.5. Model Results and Data Analysis

In this section we present the dayside helium density profile as a function of altitude, which we obtained from our ab-initio steady-state model and compare it to the ICW-derived in situ density measurements from Weichbold et al. (2025). This comparison is shown in Figure 3.

The measurement set considered here spans a timeframe of 4 years and samples a wide range of altitudes, latitudes and local times. Since ICW events are detected through magnetospheric disturbances of the upstream IMF, the resulting abundance measurements are limited to exospheric regions above the dayside and outside the bow shock. Due to the relatively sparse sampling of these large temporal and spatial domains, the data set is not necessarily well suited for resolving potential seasonal and spatial trends, and thus the modeling efforts presented in this section is focussed on capturing the global steady state of the system under averaged conditions. For a more detailed explanation of measurement principles and limitations the reader is referred to the publication by Weichbold et al. (2025).

The ab-initio model of the steady-state dayside exosphere matches the data very well. This is the case for both the intercept as well as the slope of the curve, which suggests that the implementation of the model indeed captures the driving mechanisms of the helium exosphere. This is further illustrated by the statistics of the residuals, which approximately follow a log-normal distribution, as shown in Figure 4. If one were to conceive arbitrary density profiles with the goal of better fitting the data, one could consider a density profile with smaller n_0 and flatter slope, which can produce similar or better residual statistics. However, the latter would require more energetic processes to release the He into the exosphere than thermal release, and as elaborated upon in the discussions of

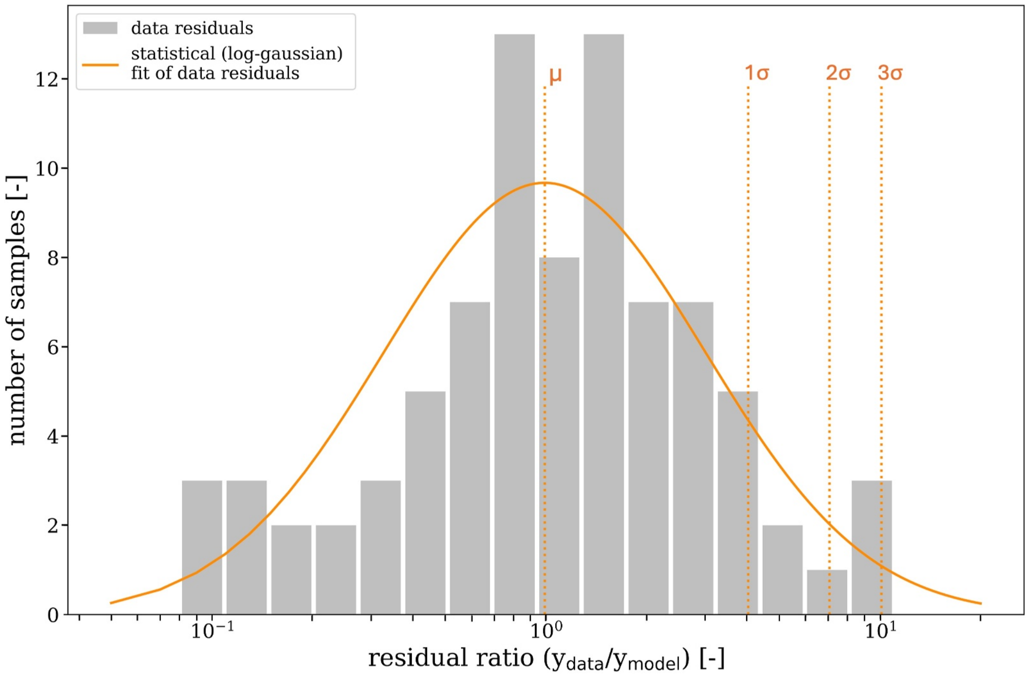

Figure 4. Statistics of residuals (as ratio) from the model and data comparison.

Section 2.1 and the work referenced therein, there are no such processes that act on the helium particles consistently and at a large enough scale.

The residual statistics allow us to conclude that the ICW-derived density measurements are consistent with a solar wind driven helium exosphere and that the thermal recycling of previously released helium is the dominant flux in the helium exosphere. However, the comparison in Figure 3 and the distribution of residual ratios in Figure 4 shows a large spread of the measurement around the modeled steady-state He density profile. This is not surprising, since the data are collected over a 4-year period, spanning multiple hermean seasons and being collected over different latitudes and local times.

In addition to the seasonal and local time variability, such as the aforementioned peak of the interstellar wind contribution, there are mechanisms which can temporarily induce change in the strength of the helium source and helium loss rates. Examples of such are the variability in solar wind composition as a function of the origin of the plasma (e.g., fast streams originating from coronal holes have He^{++} abundance fractions $< 5\%$) and the variations in solar emission intensity in the photo-ionizing wavelengths. Reduced source strength can be accounted for by for example, reduced solar wind flux, poor penetration efficiency of the ions to the surface or He^{++} precipitation onto unsaturated geographic locations, where implantation does not demand release of a source flux particle. Furthermore, the implantation efficiency may vary with local geographic properties (e.g., local surface magnetic signatures (Vorburger et al., 2012) or mechanical properties), such that precipitation in certain areas may lead to much increased back-scattering of the ions as energetic neutrals, which due to their large kinetic energy will escape the exosphere and thus do not contribute as exospheric source flux. Contrary, increased ion precipitation and implantation during for example, the collapse of the bow shock or large magnetospheric re-connection events can strengthen the helium source (Fatemi et al., 2020). Helium escape loss rates, which in our model are directly coupled to the surface temperature (Section 2.1) do not undergo significant variations with the seasonal variability of the hermean equilibrium temperature. Ionization loss rates however can be affected by varying solar emission intensity in the photo-ionizing wavelengths.

Local density measurements are however dominated by the exospheric recycling and do not directly resolve the local source flux. This suggests that the variability in the measured helium abundance is not due to locally varying source flux, but rather reflects a depletion or enrichment of exospheric helium on a global level. When considering global exospheric trends, one must consider the inertia of the global exosphere. The scale time of exospheric decay is in the order of the average exospheric lifetime of a helium particle, for which different authors give widely different quantities: in a preliminary estimate Broadfoot et al., 1974 give a lifetime of ≈1 day, Hartle et al., 1975 corrected this to some 200 days, while most recently Quémerais et al. (2023) claim the value to be ≈10 days. Combining the average time-of-flight and the effective recycle factor given by our model, we obtain an average exospheric lifetime of ≈50 days. Assuming that the true scale time is some tens of days, depleting or enriching processes need to be sustained over comparable time scales to effectuate substantial variations in the global helium levels. The recent observations of He by BepiColombo reported by Quémerais et al. (2023) find that the earlier Mariner 10 He densities at the surface are a factor 4.5–7.5 higher than they derived. This suggests that possibly there is a large variation in the global helium densities.

The comparison of the He measurements with our model (Figure 3) and the distribution of ratios between observation and model (Figure 4) show that the He densities measured locally over the 4-year timespan have variations of ± factor 4 in 1-σ and ± factor 10 in 3-σ. While part of the deviating data can still be explained by the model within the cumulative uncertainty, there still remains a number of measurements that cannot be consolidated with the model. Due to the complexity of the underlying mechanisms it is difficult to evaluate if variations in the helium source can be sustained at such high levels over some tens of days to cause such substantial deviations from the steady state on a global scale, but as we argue in Section 2.1 this seems unlikely. This suggests, that at least the most extreme deviations from the expected average abundance could in fact be decoupled from the global helium abundance, that is, are caused by mechanisms that effectuate extreme local depletion or enrichment. The nature of local depletion mechanisms is unclear and has not yet been discussed in literature. Local enrichment of the helium abundance could be caused by meteoroid impacts, where helium can be released in large quantities from the vaporised and heated regolith. This mechanism and its signature in the helium exosphere is studied in Section 3.

3. Meteoroid Impact Signatures in the Helium Exosphere

In the analysis of the residual distribution (Section 2.5) it was noted that despite the long exospheric decay time (order of tens of days) the spread of measured densities spans two orders of magnitude around the expected average level (see Figures 4 and 3-σ range), suggesting that at least the most extreme of the measured deviations could be of local nature and decoupled from the steady-state He exosphere. In this section we investigate the meteoroid impact vaporization mechanism as a possible source for measurably enriched local helium abundance in Mercury's exosphere. We focus on the large impact events with projectile radii of approximately one m, because these are the largest objects that have a reasonable probability to occur during the observation period of 4 years (Marchi et al., 2005).

In Section 3.1 we describe our approach for the modeling of meteoroid impact signatures. In Section 3.2 we discuss the probabilistic aspects of detecting such a signature and try to relate this analysis to the helium density measurements from Weichbold et al. (2025).

3.1. Modeling Meteoroid Impact Signatures

Besides the steady flux of micrometeoroids (Cintala, 1992), large impactors (diameter > 10^{-2} m), mostly originating from the main asteroid belt, are expected to impact on Mercury (Marchi et al., 2005). While the role of these larger meteoroids as a driver for the global hermean exosphere is negligible compared to the contribution of micrometeoroid impact (Cremonese et al., 2005), they could cause a local and transient increase in the exospheric density. Mangano et al. (2007) have shown that in the number density of some species such as Ca, Na, K and O one can expect a detectable signature from the impact of meteoroids of 1 m size. For the modeling of the meteoroid impact signature in the helium exosphere we adopt an approach similar to theirs.

First, the bulk abundance of helium in the hermean regolith needs to be established. By using the mechanical and structural analogy with the Lunar regolith (Broadfoot et al., 1974; McCord & Adams, 1972; Murray et al., 1974), we assume that hermean regolith saturates in helium at similar abundance levels. The analysis of lunar soil and regolith breccia samples from the Apollo and Luna missions showed helium abundances around 10 wppm, with some samples reaching as high as 100 wppm (Heiken et al., 1991). For the mean helium abundance in the hermean regolith we will assume a value of 10 wppm, which using a mean atomic mass of the hermean regolith at 24.4 (Evans et al., 2012) is equivalent to 60 ppm. It should be emphasized that these abundances refer to the regolith in bulk.

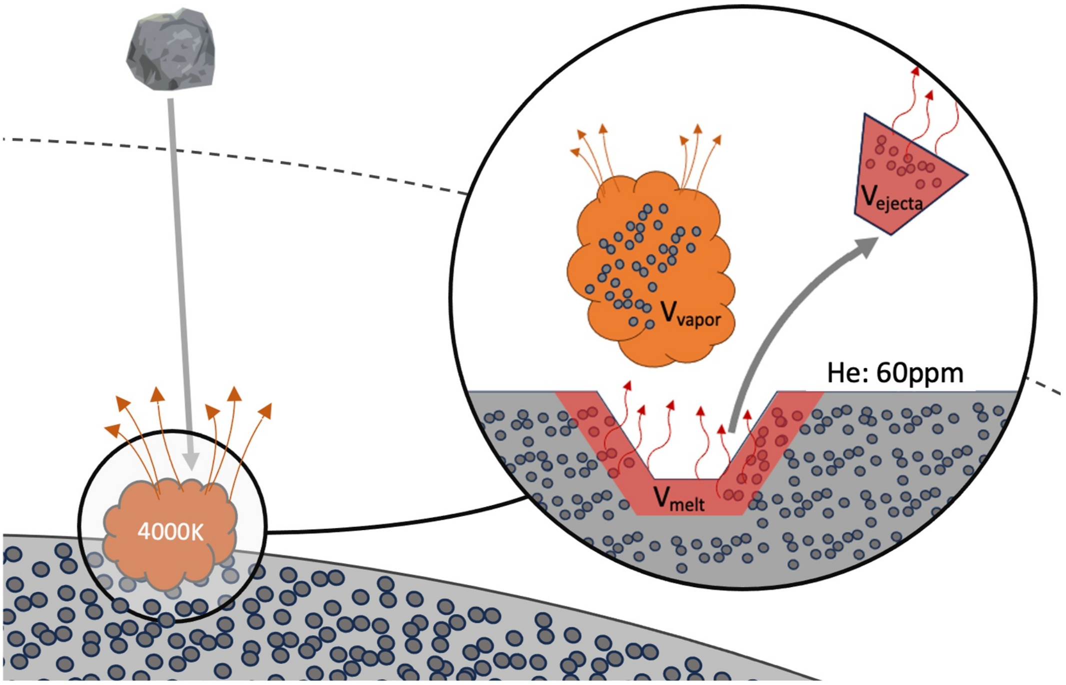

Figure 5. Schematic depiction of the helium release during an impact event. The release is modeled as a thermal cloud at 4,000 K. The released helium originates from the vaporised regolith (V_{vapor}), but at least partial outgassing from the heated and shocked melted and ejected regolith should be considered.

To determine the amount of helium that is released into the exosphere during such impact, we proceed analogous to the modeling of exospheric supply from micrometeoroid impact vaporization (Wurz & Lammer, 2003). This supply mechanism is schematically shown in Figure 5. At the impact site, the regolith undergoes transformation: we consider the creation of a vapor phase, a melt phase and solid ejecta. The mass contained in each partition can be calculated using analytical formulas from for example, Holsapple (1993) and Cintala (1992). We adopt the formulations of Holsapple (1993), since they are most applicable to the 0.01–1 m impactor size regime. The dynamics of the particle release are modeled as a thermal process, with an average temperature of the released material of 4000 K (Eichhorn, 1978).

In models of exospheric supply from meteoroid impacts, the amount of material released into the exosphere is the vapor partition of the impacted regolith (Cintala, 1992, e.g.), which is sufficient when applied to the study of refractory species that do not easily diffuse from heating of the regolith. However, in the case of a highly volatile species such as helium, which easily diffuses from heated regolith, it is worth considering that He supplied to the exosphere might also be released from the melted volume of the impact, and from the ejecta volume. From the study of noble gases in meteoroids we know that all implanted noble gases are released by heating these minerals up to about 2100 K (Eugster et al., 1993). Thus, it seems plausible to assume that at least part of the helium in the impact melt and impact ejecta partition are released into the vapor phase as a consequence of the extreme heating and shock during impact (Carrier III et al., 1973; Stöffler & Keil, 1991). This effectively leads to a significant enrichment of helium in the vapor phase for meteoroid impacts. Considering the ratio of the melt and ejecta mass over the vapor mass (Table 2), the enrichment of the vapor phase with helium from the other partitions can be significant. Given the temperature of the impact plume of about 4,000 K (Eichhorn, 1978) it is plausible that most helium will escape the regolith when melted and thus the considered helium yield should include vapor and melt partition. How much additional helium is released from the ejected material is difficult to constrain. However, it is likely that there is partial release of He from the ejecta, given the high temperatures during this process.

In summary, it must be admitted that there are large uncertainties related to the helium release from impact events. These uncertainties stem from the uncertainty of the helium source partition and from inferring helium bulk abundance by lunar analogy. To account for this, we introduce the enrichment factor f, which we will carry forward as a free parameter. The parameter denotes the enrichment of the helium release during impact with respect to the baseline He release, which is obtained by applying the 60 ppm abundance on the volume of the vaporised partition. Assuming the bulk abundance to be accurate within a factor ± 2 and restricting the partial helium release from the solid partition to small (1%) and moderate (10%), the possible value for f are between 0.5 and 60, where we consider the range of likely values between 3 and 30.

Just like Mangano et al. (2007), we adopt the probability distribution as function of impactor size and velocity from Marchi et al. (2005). According to these distributions, impactors with diameter >1 m can be expected at a rate of 2 per year and their most probable velocity is 40 km/s. We use the Lunar Cratering Tool (Holsapple, 2007) to retrieve the vaporised, melted, and ejecta yield of such an impact. The results are shown in Table 2.

Table 2
Yields of Excavated Material By a Rocky 1 m Diameter Meteoroid, Impacting Perpendicular on the Surface at 40 km/S

	Vapor phase	Melt phase	Solid phase (ejecta)
mass yield (kg)	3.28×10^4	6.86×10^4	8.88×10^6
yield ratio (vapor masses)	1	≈2	≈270
He yield (number count)	4.74×10^{27}	9.91×10^{27}	1.28×10^{30}

Note. These calculations were made using the Lunar Cratering Tool.

The spatial and temporal evolution of the impact yield is modeled with a similar Monte-Carlo approach as is used for the calculation of exospheric density profiles (Section 2.2). A population of test particles is drawn from a Maxwell-Boltzmann distribution with mean temperature 4,000 K and their trajectories under the influence of gravity are calculated. The trajectories are then evaluated on a grid across 3 spatial dimensions and time, which allows a reconstruction of the number density evolution with time around the impact site. These simulations yield a hemispherically expanding cloud of the impact released helium, with peak densities close to the radial axis above the impact site.

We consider the helium release from the vapor mass, simulate its expansion and evaluate the density evolution at 10,000 km altitude at a maximum angular separation of ±10° from the radial axis (Figure 6). Comparison with the steady-state density levels at this altitude shows that a 1 m impactor event can indeed produce enhancements far above the local steady-state density. At this altitude and within ±10° above the impact site the density enhancement is visible (i.e., above steady-state density) for approximately 15,000 s (about 4 hr). Considering the melt and solid phase as additional helium source volumes, the amount of helium released is larger (Table 2) and the density evolution profiles scale with the ratio of the helium source volumes.

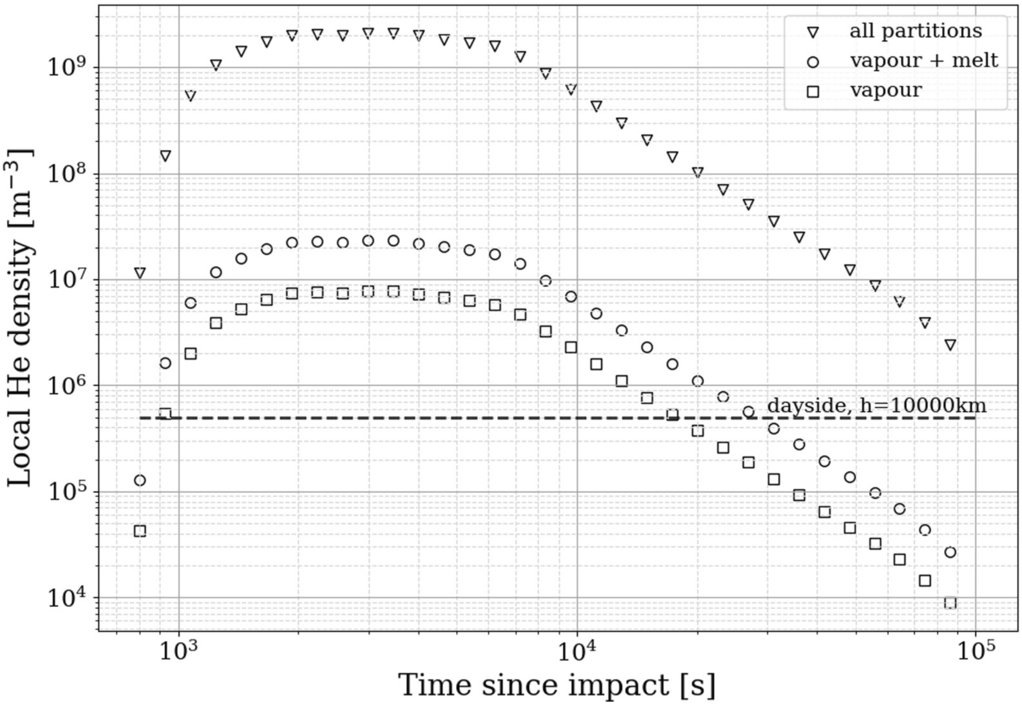

Figure 6. Local helium density at 10,000 km within ±10° from the impact location. The figure includes the local density evolution for helium release from the vapor partition, from vapor and melt, and from all partitions, with respect to the local steady-state He density.

3.2. Detectability of Impact Signatures

To examine if the most extreme ICW density measurements (≈ factor 10) could be the signature of large impact events, we need to consider two additional aspects. These considerations also extend to understanding the likelihood of detecting such impact events with in situ density measurements in general.

The first consideration addresses the criteria for identification of such impact events from in situ density measurements. Figure 6 suggests that a large impact event can lead to a temporal and local exospheric enrichment above the background and is therefore detectable. However, depending on the timing and spatial placement of the measurement with respect to the impact, the in situ measurement may only be moderately above background, which cannot be clearly attributed to a localized helium enrichment that is decoupled from the global helium abundance. Of course, a time series of in situ measurements, potentially also from other species, can be used to infer from context if the detected enrichment is coupled to the global state of the exosphere, but in case of the sporadic measurement distribution of the ICW data this is not possible. For this reason, and because the ICW data points in question are approximately by a factor of 10 above the steady-state density, we define a detectability criteria for impact events from in situ measurements, which demands that the measured density is at least 10× the expected value of the steady-state density. When considering the 10× contour in the hemispherically expanding cloud of vaporised helium, it approximately traces out a conical shape. This is illustrated by Figure 7. We conclude that the volume in which a detection of the impact by in situ measurement is possible is best modeled as a cone with its apex on the impact site, a given angular extent and finite lifetime.

The probability of in situ detection of an impact is the probability of the spacecraft to cross through the conical feature during the cone's lifetime. In the case of the ICW measurements, only feature crossings outside the bow shock result in a detection. While there exist analytical approaches for the computation of this probability (Mangano et al., 2007), we use a Monte Carlo approach. In a 3D simulation, we model the trajectory on which the detecting spacecraft is orbiting Mercury. Then, a large number (500,000) of conical features is initialized on the surface of Mercury, where the location of the apex is chosen proportional to the geometric impact probability (latitude-dependent $\propto \cos(\theta)$). For the lifetime of the cone, the spacecraft is propagated on its orbit. If a crossing of the spacecraft through the conical volume is recorded and it is compliant with additional constraints (i.e., outside the typical bow-shock boundary), it is counted as a detection. From the statistics of the Monte Carlo simulation, the detection probability can be inferred. In the case in which the lifetime of the cone is smaller than the orbital period of the spacecraft, the simulation is extended to a nested Monte Carlo. This means that for each initialization of the cone, the spacecraft is initialized 100 times in different sections of its orbits (proportional to the likelihood of finding the s/c in given section), while the overall amount of cone samples is reduced by a factor of 100 for the sake of keeping computational cost constant.

We found that for a given orbital geometry, like the orbit of the MESSENGER spacecraft, the probability of detection is a function of the angular extent and lifetime of the impact plume. These probabilities were computed over a range of these cone parameters and plotted as a contour on Figure 8. The angular extent and lifetime of the conical signature is a strong function of the amount of helium that is released from the impact. For the reasons described in Section 3.1 there is a large amount of uncertainty on this quantity and thus the vapor phase enrichment factor f was introduced as a free parameter. For a set of values of f, the angular extend and lifetime of the resulting detectability cone was computed and projected on top of the detection probability grid in Figure 8.

The synergy of cone properties as a function of released helium and the probability of crossing through such cones from the MESSENGER orbit allows us to comment on the likelihood that the ICW measurements at 10× above the average steady-state density are the signature of large impact events. First, we establish that the expected value for the amount of such impacts over the 4 years data-collection period is 8 (Marchi et al., 2005). If one of these events was captured by the data, the probability of detecting an impact signature was 1/8. Figure 8 shows, that a helium release of ≈50 times the expected release from the vapor partition is required to create a signature with a 1/8 probability of detection. Analogously, if two of the large impact events are to be detected, the expected detection probability of the signature is 1/4, which requires a helium release at an vapor phase enrichment of at least $f = 100$.

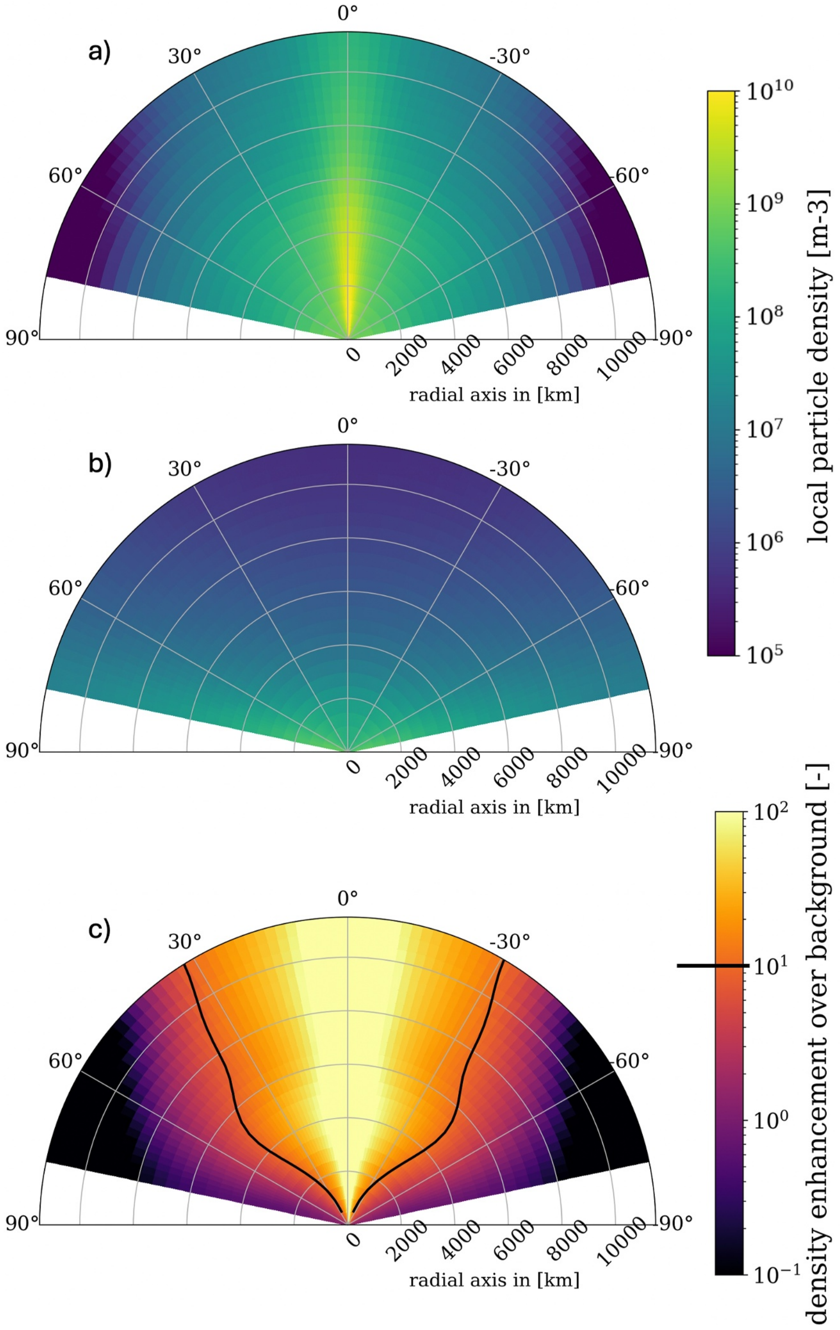

Figure 7. Expansion of the helium release cloud and geometry of its detectable signature. Panels (a, b) shows the local helium particle density from (a) meteoroid impact release and (b) the dayside steady-state density. Panel (c) shows the local density enhancement factor, as the ratio between (a, b). The detection criteria at 10× is marked with the black contour line, showing an approximately conical shape. This figure is based on the state of the local exosphere 2,000 s after the impact of a 1 m meteoroid, using a vapor phase enhancement of $f = 20$.

4. Discussion and Conclusion

We derived a simplified, semi-analytical model using an ab-initio approach and demonstrate its applicability to the cross-seasonal average steady state of the Mercury's helium exosphere by comparison with the ICW derived in situ density measurements from Weichbold et al. (2025).

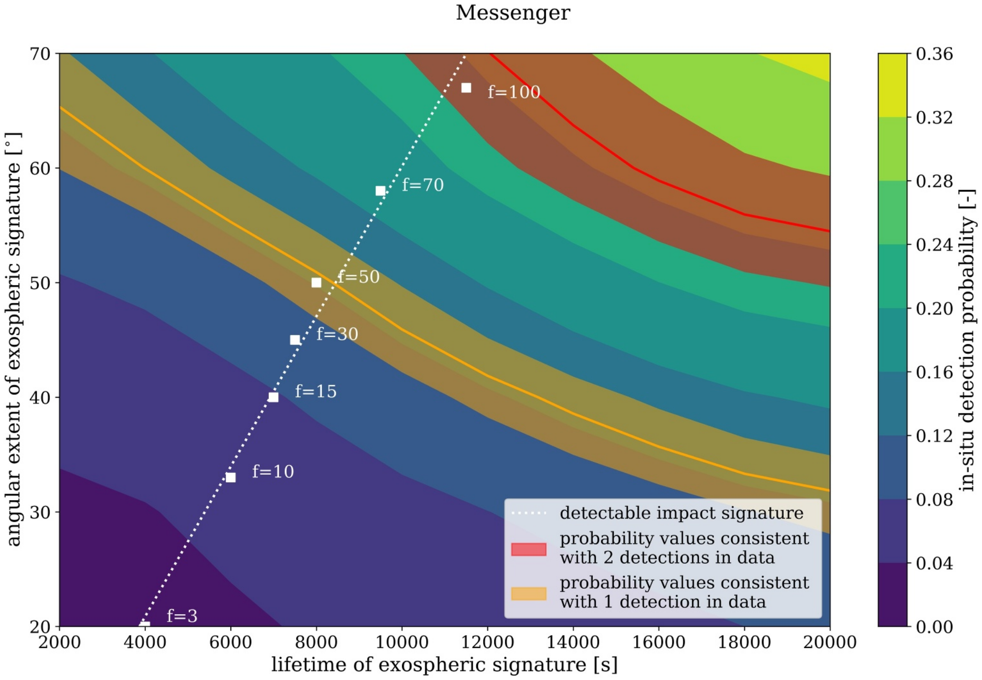

Figure 8. Resolve apparent contradiction between single and dual detection probability bands. Contours show the in situ detection probability of an impact event in exospheric helium, as a function of geometrical extent and the lifetime of the plume. The highlighted bands mark exactly one and two expected detections within 1-σ, respectively. The white points show the properties of the exospheric He signature (in the angular extend-lifetime space) as a function of the vapor phase enrichment factor f for a 1 m sized impactor. The dashed white line is a visual aid for the trend of parameter f in the angular extend-lifetime space.

The excellent agreement between the radial density profile of the ab-initio model and the altitude profile of the in situ measurements confirms that the measurable helium exosphere is dominated by the flux of thermally recycled particles. The comparison of the model result and measurements also confirmed that a source strength of.

$2.5\,^{+2.5}_{-1.25} \times 10^{23}$ He/s, which we derive from estimates of the solar wind He^{++} precipitation, supplies sufficient helium to the system.

We discussed the large spread of the in situ density measurements from Weichbold et al. (2025) and the possibility of local depletion and enrichment processes, which could account for the most extreme measurements. We investigate extreme (10×) local enrichment through large impact events and conclude that such events create detectable signatures in the helium exosphere. Due to the large uncertainty associated with the amount of helium released from impact vaporization (vapor phase enrichment, bulk abundance) it is difficult to draw definitive conclusions with respect to any individual data points. We show, however, that in the case of the ICW measurements from MESSENGER, an enrichment factor of $f \approx 50$ is needed for a single detection of a large impact event to be statistically likely during the 4 years of observations for an 1 m impactor arriving 2 times per year.

This is out of bounds of what we consider a likely value for the helium release enrichment factor f, and therefore we conclude that statistically it is not expected to have one such event signature in the data. The same holds true to a more extreme extent for two detections in the data, where the helium enrichment needs to be $f \approx 100$. We conclude that the detection of impact events in the data is unlikely, but given the small sample size, which characterizes the statistical considerations above, we cannot entirely rule out its statistical feasibility.

The uncertainties captured by the f factor and ultimately the impact vaporization dynamics of the highly volatile compounds of the hermean regolith will be better constrained by the evaluation of the in situ helium measurements of the STROFIO mass spectrometer on board the BepiColombo Mercury Planetary Orbiter (MPO) spacecraft (Orsini et al., 2021). As is shown in Appendix A, an in situ detection of an impact signature in the helium measurements of STROFIO is probable, with detections in the nightside exosphere being much more likely than on the dayside. The addition of measurements across other species (Mangano et al., 2007) and the context of the time series will allow for a more definitive identification and more detailed characterization of the exospheric signature of large impact events.

Appendix A: Analogous Detection Probability Analysis for BepiColombo

We used the computational infrastructure deployed in Section 3.2 to conduct an analogous analysis for an impact detection in the helium exosphere from the BepiColombo mission. The mission is composed of two simultaneously operating spacecraft, the MPO and the Mercury Magnetospheric Orbiter (MIO). The MPO is equipped with the STROFIO mass spectrometer (Orsini et al., 2021), thus a direct detection of the impact signature in the helium signal will be possible. Such detections can be made irrespective of orbital geometry, that is, from above both sides of the terminator. The MIO spacecraft cannot measure helium directly, but could infer the abundances from magnetic field signatures, similar to the ICW data (Weichbold et al., 2025). Just like the ICW measurements, its detection capabilities are limited to the dayside.

We computed the detection probabilities for each spacecraft separately and display them together with the extent of the impact signature in Figure A1. Note that the extent of the impact signature and how it evolves with the enhancement factor *f* varies between the two subfigures, because the signature is evaluated with different maximum altitudes (MPO: 1,500 km, MIO: 12,000 km) in mind. This can be understood when considering the bottom panel of Figure 7: an orbiter at maximum 4,000 km altitude sees an impact signature of wider angular extent than an orbiter at 10,000 km. Similar differences can be observed in the temporal extent, where at lower altitudes the impact signatures are much more short-lived.

Furthermore, it should be noted that Figure A1 only addresses the probabilities of a dayside detection. As discussed before, this is sufficient for MIO, because ICW measurements are not possible on the nightside, but we do need to consider the nightside detections of MPO. The probability of in situ detection of a cone of given spatial and temporal extent is on the nightside no different than on the dayside, but due to the different steady-state He density profiles (high density close to the surface, but very low densities at s/c orbital altitudes) the extent of the exospheric signature from a nightside impact event is much larger and longer-lived. Irrespective of the magnitude of *f*, the signature of a nightside impact can be modeled as a cone of half-angle 85° with lifetimes much larger than the MPO orbital period (>8,500 s). Such features have a detection probability of 0.7, so assuming that the occurrence of day- and nightside impacts are equally likely, the probability of a nightside detection is 0.35. The total MPO detection probability is of course the sum of day and nightside detection, but within the likely bounds of the release enhancement factor *f* (<30), dayside detection probabilities are comparatively small (0.02–0.10). With an expected 4 impact events (Marchi et al., 2005) over the 2 year extended lifespan of MPO, we therefore have an expected value of >1 for the amount of direct impact signature detection from MPO.

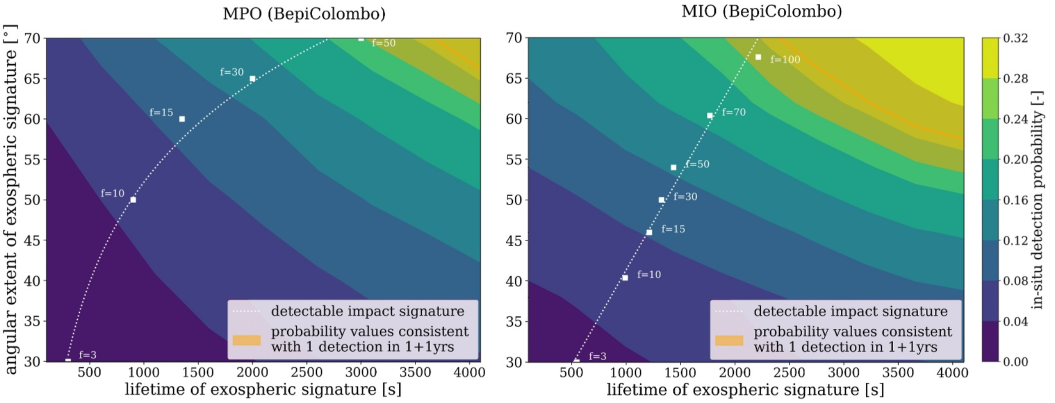

Figure A1. Extent of the impact signature and associated detection probabilities from BepiColombo's Mercury Planetary Orbiter (MPO) and MIO orbits. Note that a total detection probability over the mission cannot be obtained from summing the individual detection probabilities of MPO and MIO, because the two spacecraft are in co-planar orbits and thus their detection probabilities for a given feature are correlated.

Data Availability Statement

All data produced in this work are open access. It is stored and documented and can be retrieved from an openly accessible repository (Hener, 2025).

Acknowledgments

J. Hener, A. Vorburger and P. Wurz gratefully acknowledge the financial support by the Swiss National Science Foundation (Grant #200020_207409).

References

Bogard, D., Nyquist, L., Hirsch, W., & Moore, D. (1973). Trapped solar and cosmogenic noble gas abundances in apollo 15 and 16 deep drill samples. *Earth and Planetary Science Letters*, *21*(1), 52–69. https://doi.org/10.1016/0012-821x(73)90225-2

Broadfoot, A., Kumar, S., Belton, M., & McElroy, M. (1974). Mercury's atmosphere from mariner 10: Preliminary results. *Science*, *185*(4146), 166–169. https://doi.org/10.1126/science.185.4146.166

Broadfoot, A., Shemansky, D., & Kumar, S. (1976). Mariner 10: Mercury atmosphere. *Geophysical Research Letters*, *3*(10), 577–580. https://doi.org/10.1029/gl003i010p00577

Carrier III, W. D., Bromwell, L. G., & Martin, R. T. (1973). Behavior of returned lunar soil in vacuum. *Journal of the Soil Mechanics and Foundations Division*, *99*(11), 979–996. https://doi.org/10.1061/jsfeaq.0001966

Cintala, M. J. (1992). Impact-induced thermal effects in the lunar and mercurian regoliths. *Journal of Geophysical Research*, *97*(E1), 947–973. https://doi.org/10.1029/91je02207

Cremonese, G., Bruno, M., Mangano, V., Marchi, S., & Milillo, A. (2005). Release of neutral sodium atoms from the surface of mercury induced by meteoroid impacts. *Icarus*, *177*(1), 122–128. https://doi.org/10.1016/j.icarus.2005.03.022

Eichhorn, G. (1978). Primary velocity dependence of impact ejecta parameters. *Planetary and Space Science*, *26*(5), 469–471. https://doi.org/10.1016/0032-0633(78)90068-5

Eugster, O., Michel, T., Niedermann, S., Wang, D., & Yi, W. (1993). The record of cosmogenic, radiogenic, fissiogenic, and trapped noble gases in recently recovered Chinese and other chondrites. *Geochimica et Cosmochimica Acta*, *57*(5), 1115–1142. https://doi.org/10.1016/0016-7037(93)90045-X

Evans, L. G., Peplowski, P. N., Rhodes, E. A., Lawrence, D. J., McCoy, T. J., Nittler, L. R., et al. (2012). Major-element abundances on the surface of mercury: Results from the messenger gamma-ray spectrometer. *Journal of Geophysical Research*, *117*(E12). https://doi.org/10.1029/2012je004178

Fatemi, S., Poppe, A., & Barabash, S. (2020). Hybrid simulations of solar wind proton precipitation to the surface of mercury. *Journal of Geophysical Research: Space Physics*, *125*(4), e2019JA027706. https://doi.org/10.1029/2019ja027706

Goldstein, B., Suess, S., & Walker, R. (1981). Mercury: Magnetospheric processes and the atmospheric supply and loss rates. *Journal of Geophysical Research*, *86*(A7), 5485–5499. https://doi.org/10.1029/ja086ia07p05485

Grimberg, A., Bühler, F., Wieler, R., & Bochsler, P. (2009). Comparison of solar wind noble gas data from genesis with apollo/swc–new results from implantation experiments. In *40th Annual lunar and planetary science conference* (p. 1537).

Hartle, R., Curtis, S., & Thomas, G. (1975). Mercury's helium exosphere. *Journal of Geophysical Research*, *80*(25), 3689–3692. https://doi.org/10.1029/ja080i025p03689

Heiken, G. H., Vaniman, D. T., & French, B. M. (1991). *Lunar sourcebook: A user's guide to the Moon*, Cambridge.

Hener, J. (2025). Hermean helium 2025 - Jgr [Dataset]. *Zenodo*. https://doi.org/10.5281/zenodo.14924499

Holsapple, K. A. (1993). The scaling of impact processes in planetary sciences. *Annual Review of Earth and Planetary Sciences*, *21*(1), 333–373. https://doi.org/10.1146/annurev.earth.21.1.333

Holsapple, K. A. (2007). Lunar cratering calculator. Retrieved from https://www.lpi.usra.edu/lunar/tools/lunarcratercalc

Huebner, W., & Mukherjee, J. (2015). Photoionization and photodissociation rates in solar and blackbody radiation fields. *Planetary and Space Science*, *106*, 11–45. https://doi.org/10.1016/j.pss.2014.11.022

Jr Chase, S., Miner, E., Morrison, D., Münch, G., & Neugebauer, G. (1976). Mariner 10 infrared radiometer results: Temperatures and thermal properties of the surface of mercury. *Icarus*, *28*(4), 565–578. https://doi.org/10.1016/0019-1035(76)90130-5

Jr Hodges, R., & Johnson, F. (1968). Lateral transport in planetary exospheres. *Journal of Geophysical Research*, *73*(23), 7307–7317. https://doi.org/10.1029/ja073i023p07307

Jull, A., & Pillinger, C. (1977). Effects of sputtering on solar wind element accumulation. In *Lunar science conference, 8th, houston, tex., march 14-18, 1977, proceedings* (Vol. 3, pp. 3817–3833). Pergamon Press.

Kallio, E., & Janhunen, P. (2003). Solar wind and magnetospheric ion impact on mercury's surface. *Geophysical Research Letters*, *30*(17). https://doi.org/10.1029/2003gl017842

Killen, R., Cremonese, G., Lammer, H., Orsini, S., Potter, A. E., Sprague, A. L., et al. (2007). Processes that promote and deplete the exosphere of mercury. *Space Science Reviews*, *132*(2–4), 433–509. https://doi.org/10.1007/s11214-007-9232-0

Leblanc, F., & Chaufray, J.-Y. (2011). Mercury and moon he exospheres: Analysis and modeling. *Icarus*, *216*(2), 551–559. https://doi.org/10.1016/j.icarus.2011.09.028

Lord, H. (1968). Hydrogen and helium ion implantation into olivine and enstatite: Retention coefficients, saturation concentrations, and temperature-release profiles. *Journal of Geophysical Research*, *73*(16), 5271–5280. https://doi.org/10.1029/jb073i016p05271

Lue, C., Futaana, Y., Barabash, S., Wieser, M., Bhardwaj, A., & Wurz, P. (2014). Chandrayaan-1 observations of backscattered solar wind protons from the lunar regolith: Dependence on the solar wind speed. *Journal of Geophysical Research: Planets*, *119*(5), 968–975. https://doi.org/10.1002/2013JE004582

Lue, C., Futaana, Y., Barabash, S., Wieser, M., Holmström, M., Bhardwaj, A., et al. (2011). Strong influence of lunar crustal fields on the solar wind flow. *Geophysical Research Letters*, *38*(3). https://doi.org/10.1029/2010GL046215

Mangano, V., Milillo, A., Mura, A., Orsini, S., De Angelis, E., Di Lellis, A., & Wurz, P. (2007). The contribution of impulsive meteoritic impact vapourization to the hermean exosphere. *Planetary and Space Science*, *55*(11), 1541–1556. https://doi.org/10.1016/j.pss.2006.10.008

Marchi, S., Morbidelli, A., & Cremonese, G. (2005). Flux of meteoroid impacts on mercury. *Astronomy and Astrophysics*, *431*(3), 1123–1127. https://doi.org/10.1051/0004-6361:20041800

Massetti, S., Orsini, S., Milillo, A., Mura, A., De Angelis, E., Lammer, H., & Wurz, P. (2003). Mapping of the cusp plasma precipitation on the surface of mercury. *Icarus*, *166*(2), 229–237. https://doi.org/10.1016/j.icarus.2003.08.005

McCord, T. B., & Adams, J. B. (1972). Mercury: Interpretation of optical observations. *Icarus*, *17*(3), 585–588. https://doi.org/10.1016/0019-1035(72)90024-3

Murray, B. C., Belton, M. J., Danielson, G. E., Davies, M. E., Gault, D. E., Hapke, B., et al. (1974). Mercury's surface: Preliminary description and interpretation from mariner 10 pictures. *Science*, *185*(4146), 169–179. https://doi.org/10.1126/science.185.4146.169

Orsini, S., Livi, S., Lichtenegger, H., Barabash, S., Milillo, A., De Angelis, E., et al. (2021). Serena: Particle instrument suite for determining the sun-mercury interaction from bepicolombo. *Space Science Reviews*, *217*, 1–107. https://doi.org/10.1007/s11214-020-00787-3

Quémerais, E., Koutroumpa, D., Lallement, R., Sandel, B. R., Robidel, R., Chaufray, J.-Y., et al. (2023). Observation of helium in mercury's exosphere by phebus on bepi-colombo. *Journal of Geophysical Research: Planets*, *128*(6), e2023JE007743. https://doi.org/10.1029/2023je007743

Shemansky, D., & Broadfoot, A. L. (1977). Interaction of the surfaces of the moon and mercury with their exospheric atmospheres. *Reviews of Geophysics*, *15*(4), 491–499. https://doi.org/10.1029/rg015i004p00491

Smith, E. V., & Gottlieb, D. M. (1974). Solar flux and its variations. *Space Science Reviews*, *16*(5–6), 771–802. https://doi.org/10.1007/bf00182600

Smith, G. R., Shemansky, D., Broadfoot, A. L., & Wallace, L. (1978). Monte Carlo modeling of exospheric bodies: Mercury. *Journal of Geophysical Research*, *83*(A8), 3783–3790. https://doi.org/10.1029/ja083ia08p03783

Stöffler, D., Keil, K., & Edward R.D, S. (1991). Shock metamorphism of ordinary chondrites. *Geochimica et Cosmochimica Acta*, *55*(12), 3845–3867. https://doi.org/10.1016/0016-7037(91)90078-j

Vorburger, A., Wurz, P., Barabash, S., Wieser, M., Futaana, Y., Holmström, M., et al. (2012). Energetic neutral atom observations of magnetic anomalies on the lunar surface. *Journal of Geophysical Research*, *117*(A7). https://doi.org/10.1029/2012ja017553

Vorburger, A., Wurz, P., Barabash, S., Wieser, M., Futaana, Y., Lue, C., et al. (2013). Energetic neutral atom imaging of the lunar surface. *Journal of Geophysical Research: Space Physics*, *118*(7), 3937–3945. https://doi.org/10.1002/jgra.50337

Weichbold, F., Lammer, H., Schmid, D., Hener, J., Volwerk, M., Varsani, A., et al. (2025). Helium in mercury's extended exosphere determined by pick-up generated ion cyclotron waves. *Journal of Geophysical Research: Planets*. https://doi.org/10.1029/2024JE008679

Winslow, R. M., Johnson, C. L., Anderson, B. J., Korth, H., Slavin, J. A., Purucker, M. E., & Solomon, S. C. (2012). Observations of mercury's northern cusp region with messenger's magnetometer. *Geophysical Research Letters*, *39*(8). https://doi.org/10.1029/2012GL051472

Wittenberg, L., Santarius, J., & Kulcinski, G. (1986). Lunar source of 3he for commercial fusion power. *Fusion Technology*, *10*(2), 167–178. https://doi.org/10.13182/fst86-a24972

Wurz, P., Fatemi, S., Galli, A., Halekas, J., Harada, Y., Jäggi, N., et al. (2022). Particles and photons as drivers for particle release from the surfaces of the moon and mercury. *Space Science Reviews*, *218*(3), 10. https://doi.org/10.1007/s11214-022-00875-6

Wurz, P., & Lammer, H. (2003). Monte-carlo simulation of mercury's exosphere. *Icarus*, *164*(1), 1–13. https://doi.org/10.1016/s0019-1035(03)00123-4

Wurz, P., Whitby, J., Rohner, U., Martín-Fernández, J., Lammer, H., & Kolb, C. (2010). Self-consistent modelling of mercury's exosphere by sputtering, micro-meteorite impact and photon-stimulated desorption. *Planetary and Space Science*, *58*(12), 1599–1616. https://doi.org/10.1016/j.pss.2010.08.003